INTERNATIONAL JOURNAL FOR NUMERICAL METHODS IN FLUIDS
*Int. J. Numer. Meth. Fluids* 2006; **51**:49–76
Published online 17 November 2005 in Wiley InterScience (www.interscience.wiley.com). DOI: 10.1002/fld.1107

# Numerical prediction of a turbulent curved wake and comparison with experimental data

M. R. Mokhtarzadeh-Dehghan*,† and N. Piradeepan

*School of Engineering and Design, Brunel University, Uxbridge, Middlesex UB8 3PH, U.K.*

SUMMARY

Numerical studies of the curved wake of a NACA 0012 airfoil of chord length 0.150 m are presented. The airfoil is placed in air at 10 m/s in the straight section of a duct of 0.457 m × 0.457 m cross-section followed by a 90° bend with a mean radius-to-height ratio of 1.17. The trailing edge is located at one chord length upstream of the bend entry plane. The authors' own measurements are used to define the boundary conditions and for comparison with the predicted results.

The numerical models are based on the time-averaged, three-dimensional conservation equations of fluid flow, incorporating the $k$–$\varepsilon$, RNG $k$–$\varepsilon$, realizable $k$–$\varepsilon$ and the Reynolds stress turbulence models.

The results show that the models are capable of predicting the effects of curvature on the wake development. However, quantitative differences between prediction and experiment exist. The results obtained using the Reynolds stress model show better agreement with the experimental data, compared with the $k$–$\varepsilon$ based models, but not consistently for all parameters. There are also better predictions by the RNG $k$–$\varepsilon$ and realizable $k$–$\varepsilon$ models compared with the standard $k$–$\varepsilon$ model. The predicted results using the RNG $k$–$\varepsilon$ are closer to experimental data than the realizable $k$–$\varepsilon$. Copyright © 2005 John Wiley & Sons, Ltd.

KEY WORDS: turbulent; wake; curvature; airfoil; numerical

## 1. INTRODUCTION

Turbulent shear flows that are not directly influenced by solid walls are referred to as free shear layers. The three main types of these flows are mixing layers, jets and wakes. A wake forms behind a solid body placed in a fluid flow and therefore occurs in many practical situations. Complex wakes are subjected to extra rates of strain due to curvature and pressure gradient. An area where complex wakes form and the knowledge of wake characteristics and properties are important is aircraft aerodynamics. In multi-element wings, an element may be located in the wake of another element and therefore its performance is affected. Curved

*Correspondence to: M. R. Mokhtarzadeh-Dehghan, School of Engineering and Design, Brunel University, Uxbridge, Middlesex UB8 3PH, U.K.
†E-mail: reza.mokhtarzadeh@brunel.ac.uk

*Received 17 August 2004*
*Revised 18 April 2005*
*Accepted 5 September 2005*

Copyright © 2005 John Wiley & Sons, Ltd.

wakes also occur where guide vanes are used to direct the flow and reduce losses, as in curved ducts, or to improve aerodynamics of moving bodies and reduce drag. Turbulent wakes are also good candidates for testing numerical models, especially when they are subjected to extra rates of strain due to curvature and pressure gradient.

There have been a significant number of studies on wakes behind streamlined bodies, such as airfoils and thin plates, and behind bluff bodies, such as circular and square cylinders. But the main focus has been on wakes subjected to zero pressure gradient and zero streamline curvature. There have been only a few experimental studies of wakes subjected to curvature and pressure gradient, and even fewer numerical studies, to investigate these effects on the wake properties.

The first extensive experimental study of straight wakes was done by Chevray and Kovasznay [1]. Studies on wakes subjected to curvature, however, started much later by Savil [2] and Koyama [3] who studied the wake of a cylinder. Nakayama [4] studied the mean and turbulence quantities in the wake of a wire, subjected to mild pressure gradient and streamline curvature effects. A series of experiments were later reported by Ramjee *et al.* [5], Ramjee and Neelakandan [6, 7] and Tulapurkara *et al.* [8, 9], who used NACA 0012 airfoils and square cylinders as the wake generating body placed in a curved duct. Further studies were reported by John and Schobeiri [10], Schobeiri *et al.* [11] who used a circular rod, and Starke *et al.* [12] who used a flat plate as the wake generating body.

The previous experimental results show a number of differences between a curved wake and a straight wake. Curvature causes an asymmetry about the wake centreline in the profiles of mean and turbulence quantities. The wake-half width is greater on the inner side of the curved wake, where the inner side is the side closer to the centre of curvature. Curvature has a stabilizing effect on the outer side and a destabilizing effect on the inner side of the wake. As a result, turbulence intensities are enhanced on the inner side, but are reduced on the outer side. Turbulence shear stresses are also similarly affected.

Only a few numerical studies of wakes subjected to curvature and pressure gradient have been reported. Narasimhan *et al.* [13] predicted the wake of a NACA 0012 airfoil placed in a curved duct using the $k$–$\varepsilon$ turbulence model and compared the results with the experimental data of Ramjee and Neelakandan [7]. They also made comparisons between the results for the cases where $C\mu$ (a parameter in the $k$–$\varepsilon$ model—see Section 3) had a constant value of 0.09 (the commonly adopted *standard value*) and when it was a function of the local curvature according to a relationship given by Leschziner and Rodi [14]. In a further numerical study by Tulapurkara *et al.* [15] using the $k$–$\varepsilon$ model, comparisons were made between the predicted results and experimental data of Tulapurkara *et al.* [8] who made additional measurements of turbulence quantities for a straight wake, a wake subjected to adverse pressure gradient only, and a wake subjected to adverse pressure gradient and curvature. They incorporated, additionally, a relationship proposed by Humphrey and Pourahmadi [16], which defined $C\mu$ in terms of a curvature parameter signifying the curvature strain to shear strain ratio, and the ratio of turbulence energy production to its rate of dissipation.

In the above numerical studies, the imposition of the boundary conditions had several features, which is believed to have helped the very good agreement between the predicted results and the experimental data. Firstly, the inlet to the computational domain was set at the trailing edge of the airfoil (at $s/c = 0$, where $s$ is the streamwise distance and $c$ is the chord length). Secondly, the streamwise pressure gradient, $\partial p/\partial s$, in the momentum equation was prescribed. This parameter was obtained from the potential velocity distribution in the

Copyright © 2005 John Wiley & Sons, Ltd. 

inviscid region, outside the wake. Thirdly, the profiles of the streamwise velocity $U$, turbulence energy $k$ and energy dissipation rate $\varepsilon$ at this location (inlet) were defined in a such a way that a good match with the experimental data for the average wake half-width ($b'_{\text{avg}}$), the maximum velocity defect ($W_0$) and velocity profile was obtained at the first measurement station, which was located at one-half-chord downstream of the trailing edge ($s/c = 0.5$). The boundary conditions were also defined at the upper and lower edges of the wake for $U$, $k$ and $\varepsilon$, where $U$ was set equal to the potential velocity. Additionally, the normal velocity component $V$ was set to zero along the wake centreline.

It will be seen in Section 4 that in the present work, the boundary conditions were set at a location upstream of the airfoil and at the duct walls. Therefore, the flow about the airfoil was predicted as part of the computation.

From the previous numerical studies, the following observations can be made. The mean parameters, namely the wake half-width and the maximum velocity defect, can be predicted accurately when modifications to $C\mu$ are introduced. The increase of turbulence intensity and shear stress (qualitatively) on the inner side and the decrease of these quantities on the outer side (leading to asymmetry in the profile) can be predicted using the $k$–$\varepsilon$ model. However, to obtain close quantitative agreement with the experimental data, a higher level turbulence model is required. There is a greater difficulty to predict the turbulence quantities on the inner side, where there is always an overprediction of the peak in turbulence energy and shear stress. On the outer side, the shear stress is underpredicted, but turbulence energy can be predicted more accurately. The prediction of curvature effect is more difficult than the prediction of the effect of streamwise pressure gradient.

As a primary test, it is expected that a numerical model, which incorporates turbulence modelling, be able to predict the main characteristics of a curved wake. But it is the degree of quantitative agreement between experimental data and numerical prediction that highlights the capability of one model against the other. For a curved wake improved turbulence models to account for turbulence anisotropy and extra rates of strain due to curvature and pressure gradient are needed.

Piradeepan [17] and Piradeepan and Mokhtarzadeh-Dehghan [18] reported a detailed set of experimental data for the curved wake of a NACA 0012 airfoil. This data included measurements of mean and turbulence quantities at one chord length ($c$) upstream of the leading edge, at $1.0c$ downstream of the trailing edge, and at further three downstream locations. Additional measurements of the wake profile were carried out by Onura [19] at $c/30$ downstream of the trailing edge. Onura also obtained measurements of the boundary layer on the upper surface of the airfoil at about $0.17c$ upstream of the trailing edge. The motivation behind the present numerical work was to obtain a better understanding of a curved wake and, by comparison with the authors' own experimental data, to assess the degree of agreement that may be achieved with the results obtained from the application of existing numerical techniques and turbulence models. In the previous work reviewed above, only the standard $k$–$\varepsilon$ model was used. The contribution of the present work is in providing comparisons with new experimental data and assessment of the RNG $k$–$\varepsilon$, the realizable $k$–$\varepsilon$ and the Reynolds stress models.

## 2. THE EXPERIMENTAL FLOW

An experimental rig was set up to measure the mean and turbulence parameters of a curved wake. The wake generating body was a NACA 0012. The curvature was introduced by placing

Copyright © 2005 John Wiley & Sons, Ltd. 

the airfoil in the straight section of a duct of 0.457 m × 0.457 m square cross-section with a 90° bend. The concave and convex radii of curvature of the bend were 0.764 and 0.307 m, respectively, giving the mean radius-to-height ratio of 1.17. The air was supplied to the duct using an open return type wind tunnel. A schematic diagram of the experimental rig is shown in Figure 1. The airfoil had a chord length of 0.15 m, which spanned the whole width of the duct. It was placed in the mid-height of the duct ($y/H = 0.5$) with the chord line being parallel to the duct lower and upper walls, and the trailing edge located at one chord length upstream of the bend entry plane.

Measurements were carried out at five stations (1–5) as shown in Figure 1. The experiments reported here were carried out at air velocity of 10 m/s. Further details of the experimental set up and measurement procedures can be found in References [17, 18, 20].

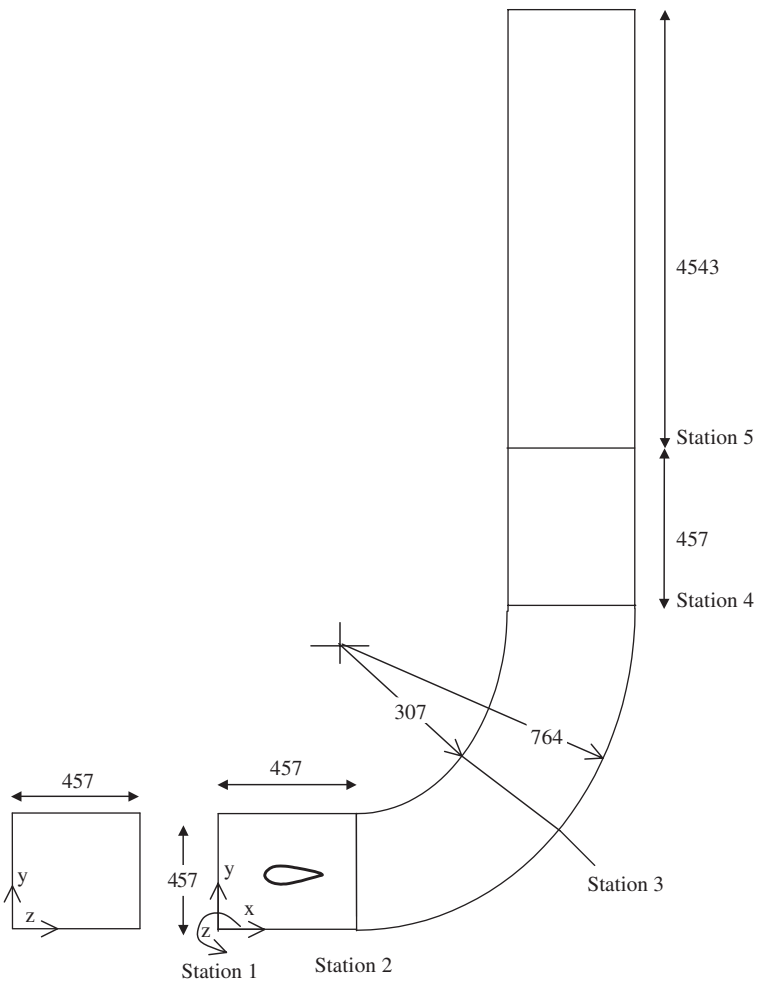


Figure 1. Schematic representation of the experimental rig (dimensions are in mm).

Copyright © 2005 John Wiley & Sons, Ltd. 

Hot-wire anemometry was used to measure the mean velocity and turbulence quantities. The static pressure distributions on the concave and convex walls in the mid-plane of the duct ($z/H = 0.5$) were measured using pressure tapping and a digital manometer.

The turbulence intensity (rms) in the free stream at station 1 was less than 0.3% of the mainstream velocity. The estimated uncertainty of the static pressure is $\pm 2\%$, mean velocity $\pm 3\%$, turbulence intensity (rms) $\pm 3\%$ and turbulence shear stress $\pm 6\%$.

The flow at station 1 was studied extensively to determine the flow condition upstream of the airfoil and for the definition of the boundary conditions. A number of spanwise profiles (fixing $y$, varying $z$) were taken to establish the flow symmetry about the duct mid-plane ($z/H = 0.5$) and the uniformity of the flow. The variations in the spanwise direction were also checked by taking a number of normal profiles in the spanwise direction (fixing $z$, varying $y$). It was concluded that the flow parameters did not change significantly in the central region, between $z/H = 0.2$ to 0.8 and, therefore, the profiles at the mid-plane provided a good basis for comparison with the numerical prediction.

## 3. MATHEMATICAL MODEL

The mathematical model is based on the time-averaged, three-dimensional, steady, incompressible conservation equations of mass and momentum (Navier–Stokes) and the equations forming the turbulence model. Four cases were studied, different only by the adopted turbulence model, namely, the standard $k$–$\varepsilon$ model, the RNG $k$–$\varepsilon$, the realizable $k$–$\varepsilon$ and the Reynolds stress model (RSM). These models are well described in the existing literature, therefore only a brief explanation is given here.

The governing equations can be written in the following general form:

$$\frac{\partial}{\partial x_i}(\rho U_i \Phi) = \frac{\partial}{\partial x_i}\left(\Gamma_\Phi \frac{\partial \Phi}{\partial x_i}\right) + S_\Phi \tag{1}$$

where $\Phi$ stands for the velocity components, $k$, $\varepsilon$ and Reynolds stresses. The term $S_\Phi$ is known as the source term. Table I shows the production and destruction terms in $S_\Phi$ for the $k$–$\varepsilon$ based turbulence models.

The standard $k$–$\varepsilon$ models are based on the eddy viscosity hypothesis by which the Reynolds stresses are obtained from the Bousinessq hypothesis

$$-\rho\overline{u_i v_j} = \mu_t\left(\frac{\partial U_i}{\partial x_j} + \frac{\partial U_j}{\partial x_i}\right) - \frac{2}{3}(\rho k \delta_{ij}) \tag{2}$$

In the *standard* $k$–$\varepsilon$ model, the eddy viscosity is obtained from

$$\mu_t = C\mu\rho\frac{k^2}{\varepsilon} \quad \text{where } C\mu = 0.09 \tag{3}$$

which is valid for high Reynolds number flows.

The RNG model was derived using the renormalization group theory [22]. In the RNG model, the effective viscosity $\mu_{\text{eff}}$ is obtained from the integration of the following equation,

Copyright © 2005 John Wiley & Sons, Ltd. 

Table I. Equations of the standard, RNG and realizable $k$–$\varepsilon$ turbulence models [21].

$$\frac{\partial}{\partial x_i}(\rho U_i \Phi) = \frac{\partial}{\partial x_i}\left(\Gamma_\Phi \frac{\partial \Phi}{\partial x_i}\right) + S_\Phi$$

| | $\Phi$ | Turbulent viscosity | $\Gamma_\Phi$ | Source term $S_\Phi$ Production | Dissipation | Constants |
|---|---|---|---|---|---|---|
| Standard $k$–$\varepsilon$ | $k$ | $\mu_t = C\mu\rho\dfrac{k^2}{\varepsilon}$ | $\mu + \dfrac{\mu_t}{\sigma_k}$ | $P_k$ | $-\rho\varepsilon$ | $c_\mu = 0.09$ |
| | $\varepsilon$ | | $\mu + \dfrac{\mu_t}{\sigma_\varepsilon}$ | $C_{1\varepsilon}\dfrac{\varepsilon}{k}P_k$ | $-C_{2\varepsilon}\rho\dfrac{\varepsilon^2}{k}$ | $\sigma_k = 1.0$<br>$\sigma_\varepsilon = 1.3$<br>$c_{1\varepsilon} = 1.44$<br>$c_{2\varepsilon} = 1.92$ |
| RNG $k$–$\varepsilon$ | $k$ | $d\left(\dfrac{\rho^2 k}{\sqrt{\varepsilon\mu}}\right) = \dfrac{1.72(\mu_{\text{eff}}/\mu)}{\sqrt{(\mu_{\text{eff}}/\mu)^3 - 1 + C_v}} d\left(\dfrac{\mu_{\text{eff}}}{\mu}\right)$ | $\alpha_k \mu_{\text{eff}}$ | $P_k$ | $-\rho\varepsilon$ | $c_{1\varepsilon} = 1.42$ |
| | $\varepsilon$ | | $\alpha_\varepsilon \mu_{\text{eff}}$ | $C_{1\varepsilon}\dfrac{\varepsilon}{k}P_k$ | $-C^*_{2\varepsilon}\rho\dfrac{\varepsilon^2}{k}$ | $c_{2\varepsilon} = 1.68$<br>$\eta_0 = 4.38$ |
| | | | | | $C^*_{2\varepsilon} = C_{2\varepsilon} + \dfrac{C\mu\rho\eta^3(1-\eta/\eta_0)}{1+\beta\eta^3}$ | $\beta = 0.012$<br>$C_v = 100$ |
| Realizable $k$–$\varepsilon$ | $k$ | $\mu_t = C\mu\rho\dfrac{k^2}{\varepsilon}$ | $\mu + \dfrac{\mu_t}{\sigma_k}$ | $P_k$ | $-\rho\varepsilon$ | $A_0 = 4.04$ |
| | $\varepsilon$ | $C\mu = \dfrac{1}{A_0 + A_s U^* \dfrac{k}{\varepsilon}}$ | $\mu + \dfrac{\mu_t}{\sigma_\varepsilon}$ | $\rho C_1 S \varepsilon$ | $-\rho C_2 \dfrac{\varepsilon^2}{k + \sqrt{v\varepsilon}}$, $v = \dfrac{\mu}{\rho}$ | $\sigma_k = 1.0$ |
| | | | | $C_1 = \max\left[0.43, \dfrac{\eta}{\eta+5}\right]$ | | $\sigma_\varepsilon = 1.2$<br>$C_2 = 1.9$ |

$P_k = -\rho\overline{u_i u_j}\dfrac{\partial U_i}{\partial x_j} = \mu_t S^2$, $S \equiv \sqrt{2S_{ij}S_{ij}}$, $S_{ij} = \dfrac{1}{2}\left(\dfrac{\partial U_i}{\partial x_j} + \dfrac{\partial U_j}{\partial x_i}\right)$, $U^* = \sqrt{S_{ij}S_{ij}}$, $A_S = f(S_{ij})$, $\eta \equiv \dfrac{Sk}{\varepsilon}$

$\alpha_k$ and $\alpha_\varepsilon$ in the RNG $k$–$\varepsilon$ are obtained using an analytical formula.

Copyright © 2005 John Wiley & Sons, Ltd.

which is derived as part of the implementation of the RNG theory [21]:

$$d\left(\frac{\rho^2 k}{\sqrt{\varepsilon\mu}}\right) = \frac{1.72(\mu_{\text{eff}}/\mu)}{\sqrt{(\mu_{\text{eff}}/\mu)^3 - 1 + C_v}}\, d\left(\frac{\mu_{\text{eff}}}{\mu}\right) \tag{4}$$

where $C_v = 100$. Equation (4) allows the low Reynolds number effects to be taken into account. At high Reynolds numbers, Equation (4) leads to Equation (3) with $C\mu = 0.0845$.

The realizable $k$–$\varepsilon$ model [23] ensures the constraint that the normal stresses ($\overline{u^2}$, etc.) remain positive (thus the word 'realizable') when the strain is large. This is achieved by making $C\mu$ to be a variable. The coefficient $C\mu$ is obtained from [21]

$$C\mu = \frac{1}{A_0 + A_s U^*(k/\varepsilon)} \tag{5}$$

where $A_0 = 4.04$. The parameters $U^*$ and $A_S$ are both functions of the mean strain rate. For the turbulent layer, the value of $C\mu = 0.09$ for high Reynolds number flows is recovered.

The production term in the $k$-equation remains the same in the three models (Table I). Apart from the way that turbulent viscosity is calculated, the differences in the three models appear in the $\varepsilon$-equation. The production terms of the $\varepsilon$-equation in the standard $k$–$\varepsilon$ and RNG $k$–$\varepsilon$ models are the same, but this term is different in the realizable $k$–$\varepsilon$; it does not contain the generation term $P_k$, instead a term $S$ which is a function of the mean strain rate. The destruction term of the $\varepsilon$-equation for all three models is different. In the standard $k$–$\varepsilon$ model the denominator of this term is $k$, which can become very small and the destruction term becomes very large. The additional term in the denominator of the destruction term in the realizable $k$–$\varepsilon$ prevents this condition to occur. Compared with the destruction terms of the standard $k$–$\varepsilon$ model and realizable $k$–$\varepsilon$ model, in which the coefficient $C_{2\varepsilon}$ is a constant, in the RNG $k$–$\varepsilon$, the equivalent coefficient $C^*_{2\varepsilon}$ can vary in response to the changes in the mean rate of strain contained in the parameter $\eta$.

Considering the above differences with the standard $k$–$\varepsilon$ model, the RNG $k$–$\varepsilon$ and realizable $k$–$\varepsilon$ model are more responsive to flows experiencing rapid strain, streamline curvature and pressure gradient.

The Reynolds stress model does not use the eddy viscosity hypothesis and obtains the turbulence stresses from their own transport differential equations. The general form of the equations for Reynolds stresses and the modelled form of these equations used in this study are shown in Table II. The energy dissipation $\varepsilon$ in the Reynolds stress equations is solved using its own equation (Table I). The RSM accounts for curvature, swirl, rotation and rapid changes in rate of strain and therefore is more accurate for complex flows. It should be noted, however, that the equations forming the RSM are a modelled form of the exact equations and therefore contain certain approximations and assumptions.

Table III shows the equations of Reynolds stresses for a two-dimensional curved shear layer in $s$–$n$ coordinates, where $s$ and $n$ are the streamwise and normal coordinates, respectively. The streamline curvature appears in the production, turbulent diffusion and pressure strain terms of these equations and therefore its effect on turbulence quantities can be deduced. These equations will be referred to again as part of the discussion.

Copyright © 2005 John Wiley & Sons, Ltd. 

Table II. The Reynolds stress transport equations.

$$\frac{\partial}{\partial x_k}(\rho U_k \overline{u_i u_j}) = P_{ij} + D_{ij}^T + \Phi_{ij} + \varepsilon_{ij} + D_{ij}^L$$

| | General form [21, 24] | Modelled terms [21] |
|---|---|---|
| Stress production $P_{ij}$ | $-\rho\overline{u_i u_k}\,\frac{\partial U_j}{\partial x_k} - \rho\overline{u_j u_k}\,\frac{\partial U_i}{\partial x_k}$ | |
| Turbulent diffusion $D_{ij}^T$ | $-\frac{\partial}{\partial x_k}[\rho\overline{u_i u_j u_k} + \overline{p(\delta_{kj}u_i + \delta_{ik}u_j)}]$ | $\frac{\partial}{\partial x_k}\left(\frac{\mu_t}{\sigma_k}\,\frac{\partial \overline{u_i u_j}}{\partial x_k}\right)$ |
| | | $\mu_t = \rho c_\mu \frac{k^2}{\varepsilon}$ |
| | | $\sigma_k = 1.0, C\mu = 0.09$ |
| Pressure strain $\Phi_{ij} = \Phi_{ij,1} + \Phi_{ij,2} + \Phi_{ij}^w$ | $\overline{p\left(\frac{\partial u_i}{\partial x_j} + \frac{\partial u_j}{\partial x_i}\right)}$ | $\Phi_{ij,1} = -c_1 \rho \frac{\varepsilon}{k}\left[\overline{u_i u_j} - \frac{2}{3}\delta_{ij}k\right]$ |
| | | $\Phi_{ij,2} = -c_2\left[\left(P_{ij} - \frac{\partial}{\partial x_k}\rho U_k \overline{u_i u_j}\right) - \frac{2}{3}\delta_{ij}\left(\frac{1}{2}P_{kk} - \frac{1}{2}C_{kk}\right)\right]$ |
| | | $c_1 = 1.8, c_2 = 0.6$ |
| | | $C_{ij} = \frac{\partial}{\partial x_k}(\rho U_k \overline{u_i u_j})$ |
| | | $\Phi_{ij}^w$ 'wall reflection', not expanded here |
| Dissipation $\varepsilon_{ij}$ | $-2\mu\overline{\frac{\partial u_i}{\partial x_k}\,\frac{\partial u_j}{\partial x_k}}$ | $\varepsilon_{ij} = \frac{2\rho}{3}\delta_{ij}\varepsilon$ |
| Molecular diffusion $D_{ij}^L$ | $\frac{\partial}{\partial x_k}\left(\mu\frac{\partial \overline{u_i u_j}}{\partial x_k}\right)$ | |

Copyright © 2005 John Wiley & Sons, Ltd.

Table III. The Reynolds stress transport equations in curvilinear $s$–$n$ coordinate system [25].

| | $\frac{\partial(U_i\Phi)}{\partial x_i} = \mathrm{SP} + \mathrm{TD} + \mathrm{PS} + D$ | | | |
|---|---|---|---|---|
| | $\Phi = \frac{1}{2}\overline{u^2}$ | $\Phi = \frac{1}{2}\overline{v^2}$ | $\Phi = \frac{1}{2}\overline{w^2}$ | $\Phi = -\overline{uv}$ |
| Stress production (SP) | $-\overline{u^2}\left(\frac{\partial U}{\partial s} + \frac{V}{R}\right)$ | $-\overline{v^2}\left(1 + \frac{n}{R}\right)\frac{\partial V}{\partial n}$ | | $\overline{u^2}\left(\frac{\partial V}{\partial s} - \frac{U}{R}\right)$ |
| | $-2\overline{uv}\,\frac{U}{R}$ | $-\overline{uv}\,\frac{\partial V}{\partial s}$ | | $+\overline{v^2}\left(1 + \frac{n}{R}\right)\frac{\partial U}{\partial n}$ |
| | $-\overline{uv}\left[\left(1 + \frac{n}{R}\right)\frac{\partial U}{\partial n} - \frac{U}{R}\right]$ | $+2\overline{uv}\,\frac{U}{R}$ | | $-(\overline{u^2} - \overline{v^2})\frac{U}{R}$ |
| Turbulent diffusion (TD) | $-\frac{\partial}{\partial s}\left(\overline{\frac{pu}{\rho}} + \frac{1}{2}\overline{u^3}\right)$ | $-\frac{1}{2}\frac{\partial}{\partial s}\overline{uv^2}$ | $-\frac{1}{2}\frac{\partial}{\partial s}(\overline{uw^2})$ | $\frac{\partial}{\partial s}\left(\overline{\frac{pv}{\rho}} + \overline{u^2v}\right)$ |
| | $-\frac{1}{2}\frac{\partial}{\partial n}\left[\left(1 + \frac{n}{R}\right)\overline{u^2v}\right]$ | $-\frac{\partial}{\partial n}\left[\left(1 + \frac{n}{R}\right)\left(\overline{\frac{pv}{\rho}} + \frac{1}{2}\overline{v^3}\right)\right]$ | $-\frac{1}{2}\frac{\partial}{\partial n}\left[\left(1 + \frac{n}{R}\right)\overline{vw^2}\right]$ | $+\left(1 + \frac{n}{R}\right)\frac{\partial}{\partial n}\left(\overline{\frac{pu}{\rho}} + \overline{uv^2}\right)$ |
| | $-\frac{\overline{u^2v}}{R}$ | $+\frac{\overline{u^2v}}{R}$ | | $+\frac{1}{R}(2\overline{uv^2} - \overline{u^3})$ |
| Pressure strain (PS) | $\overline{\frac{p}{\rho}\frac{\partial u}{\partial s}}$ | $\overline{\frac{p}{\rho}\frac{\partial}{\partial n}\left[\left(1 + \frac{n}{R}\right)v\right]}$ | $\overline{\frac{p}{\rho}\frac{\partial w}{\partial z}}$ | $-\overline{\frac{p}{\rho}\left[\frac{\partial v}{\partial s} + \left(1 + \frac{n}{R}\right)\frac{\partial u}{\partial n}\right]}$ |
| Dissipation (D) | $-\frac{1}{3}\varepsilon$ | $-\frac{1}{3}\varepsilon$ | $-\frac{1}{3}\varepsilon$ | |

Copyright © 2005 John Wiley & Sons, Ltd.

## 4. BOUNDARY CONDITIONS

At the inlet plane of the computational domain (station 1), experimentally measured profiles of the mean and turbulence quantities were set. The turbulence energy dissipation rate was calculated from

$$\varepsilon = \frac{k^{3/2}}{\ell} \tag{6}$$

where $\ell$ is a length scale. Based on the Prandtl mixing length model, the length scale within the turbulent boundary layer was taken to be equal to $\kappa y$, where $\kappa$ is the Von Kármán constant set equal to 0.41 and $y$ is the normal distance from the wall. For the region outside of the boundary layer $\ell$ was taken as $0.5\,cH$, where $c$ is a constant and $H$ is the duct height. Different values of the length scale were tried with the aim of obtaining a good match for the turbulence energy at station 2. This led to the length scale of $0.125H$, which corresponds to $c = 0.25$.

The outlet boundary was placed at $6H$ downstream of station 4. Here, the Neumann boundary condition was applied, which sets the gradients of all flow variables except pressure to zero. In the wall region, a two layer zonal model [21] was applied. In this model, the flow adjacent to the wall is divided into the near-wall region and the outer region, where the near wall region includes the viscous sublayer, buffer layer and a part of the turbulent layer. The outer region includes the rest of the flow. The boundary between these two regions is determined by the value of turbulence Reynolds number given by

$$Re_y = \frac{\rho\sqrt{k}\,y}{\mu} \tag{7}$$

where $y$ is the normal distance from the wall. For nodes satisfying $Re_y > 200$, the adopted turbulence model (e.g. RSM) is applied. For $Re_y < 200$, a one equation turbulence model is employed. In this case, the eddy viscosity is calculated from

$$\mu_t = \rho C\mu \ell_\mu \sqrt{k} \tag{8}$$

where $\ell_\mu$ is a length scale. The turbulence energy $k$ is obtained from the solution of the $k$-equation, while $\ell_\mu$ is obtained from [21, 26]

$$\ell_\mu = C_l y \left[1 - \exp\left(-\frac{Re_y}{A_\mu}\right)\right] \tag{9}$$

The dissipation of turbulence energy $\varepsilon$ is calculated from

$$\varepsilon = \frac{k^{1.5}}{\ell_\varepsilon} \tag{10}$$

where the length scale $\ell_\varepsilon$ is given by

$$\ell_\varepsilon = C_l y \left[1 - \exp\left(-\frac{Re_y}{A_\varepsilon}\right)\right] \tag{11}$$

Copyright © 2005 John Wiley & Sons, Ltd. 

In the above equations the variations of $\ell_\mu$ and $\ell_\varepsilon$ approach the linear relationship $C_1 y$ as the distance from the wall increases. The above constants are given by

$$C_l = \kappa C\mu^{-3/4}, \quad A_\mu = 70, \quad A_\varepsilon = 2C_l, \quad C\mu = 0.09, \quad \kappa = 0.418$$

When the two-layer zonal model is employed, the $y^+$ value at the cell adjacent to the wall should be ideally about 1, however, a higher value of $y^+$ value is also acceptable as long as it is less than 5 (the upper limit of the viscous sublayer).

## 5. COMPUTATIONAL DETAILS

The computational flow domain was divided into 25 blocks. These were superimposed by a structured quadrilateral grid. The final grid distribution shown in Figure 2 was obtained after extensive grid sensitivity tests. It has a total of 676 000 cells.

Grid sensitivity tests were conducted on both global and local basis. The global grid sensitivity tests first used a uniformly distributed coarse grid and the standard wall functions for the near wall treatment to obtain the overall features of the flow. The grid was then refined by gradually increasing the number of grid cells in each block in the $x$-, $y$- and $z$-directions until no significant differences of the parameters of interest were observed, particularly in the free-stream region and the near wall region of the duct. Further sensitivity tests were carried out with the two-layer zonal model and a fine grid around the airfoil, keeping the nearest grid cells to the airfoil within the viscous sublayer ($y^+ < 2$). The grid distribution around the airfoil was refined until no significant differences in the parameters of interest were resulted. On the bend walls, due to unavailability of sufficient computer memory, it was not possible

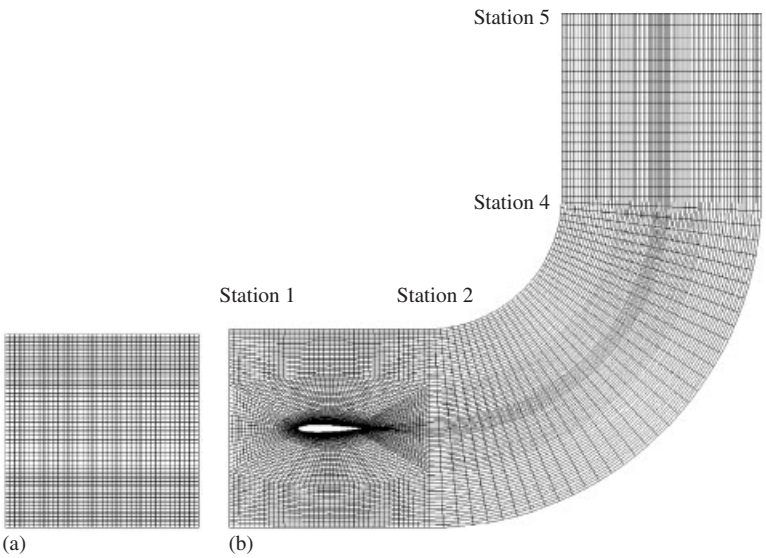


Figure 2. Computational grid (downstream of station 5 not shown): (a) cross-section at station 1; and (b) cross-section in the mid-plane.

Copyright © 2005 John Wiley & Sons, Ltd. 

to maintain the same level of fine grid employed on the airfoil. On these walls the nearest grid point was at $y^+ < 100$.

Initially, for comparison, two discretization schemes were used for the convection terms. These were the first-order upwind scheme and the third-order QUICK scheme (quadratic upstream interpolation for convective kinetics [27]). Comparison of the results with the experimental data showed a better agreement with the QUICK scheme. Therefore, this scheme was used for the results presented in this paper. The QUICK scheme uses two upstream nodes and one downstream node to determine the value of the variable at a cell face. The derivation of pressure was based on the SIMPLEC algorithm.

The following under-relaxation factors (URF) were applied. For $u$, $v$, $w$, the URF was 0.5, for $p$, 0.3, $k$ and $\varepsilon$, 0.4 and for all Reynolds stresses the URF was 0.4. The convergence solution was achieved when the scaled sum of the residuals of all variables fell below 0.001.

The solution of the linearized equations started from the initial conditions. For the $k$–$\varepsilon$ based solutions, the initialization of the solution was based on approximate (guessed) values. For the RSM solutions, however, the converged solution of the standard $k$–$\varepsilon$ was used as initial conditions.

Computations were carried out on a SUN® Sparc Ultra-60 with 2 × UltraSPARC-II 296 MHZ and 1.8 GB RAM. The standard $k$–$\varepsilon$ used the least computational effort, and the realizable $k$–$\varepsilon$ required only a little more. The RNG-$k$–$\varepsilon$ model generally took 10–15% more CPU than the standard $k$–$\varepsilon$. As expected, the RSM needed a much greater CPU and memory, and involved restarting from previous solutions. The CFD code was FLUENT 5.0.

## 6. RESULTS AND DISCUSSION

The wake centreline is defined as the locus of the minimum on the wake velocity profile. The wake centreline divides the wake into the inner side and the outer side. The wake half-width $b$ is the normal distance between the wake centreline and a point on the wake velocity profile where the velocity defect equals half of its maximum value, which occurs on the wake centreline. The total wake half-width $b'$ is the sum of the two values of $b$ corresponding to the inner side and outer side of the wake. Maximum velocity defect $W_0$ is defined as the difference between the value of velocity on the wake centreline (the minimum value) and the potential velocity also measured on the centreline, where the latter is obtained by joining the two inviscid regions with a straight line.

### *6.1. General flow description in the bend*

Before the results are presented, it is useful to describe briefly the main flow in the bend within which the wake develops. Flow in bends has been the subject of considerable study, and the flow in the present bend has also been described in the previous investigations [20]. Briefly therefore, on the convex wall, the flow accelerates in the first 45° of the bend and then decelerates in the remainder of the bend. The flow then gradually recovers, from the effects of the bend, in the downstream tangent. On the concave wall the flow is first retarded and then accelerated. The corresponding static pressure also changes accordingly. Figure 3 shows the pressure field obtained by numerical simulation. The airfoil wake therefore develops in a curved flow of non-uniform pressure field, mainly in the radial direction.

Copyright © 2005 John Wiley & Sons, Ltd. 

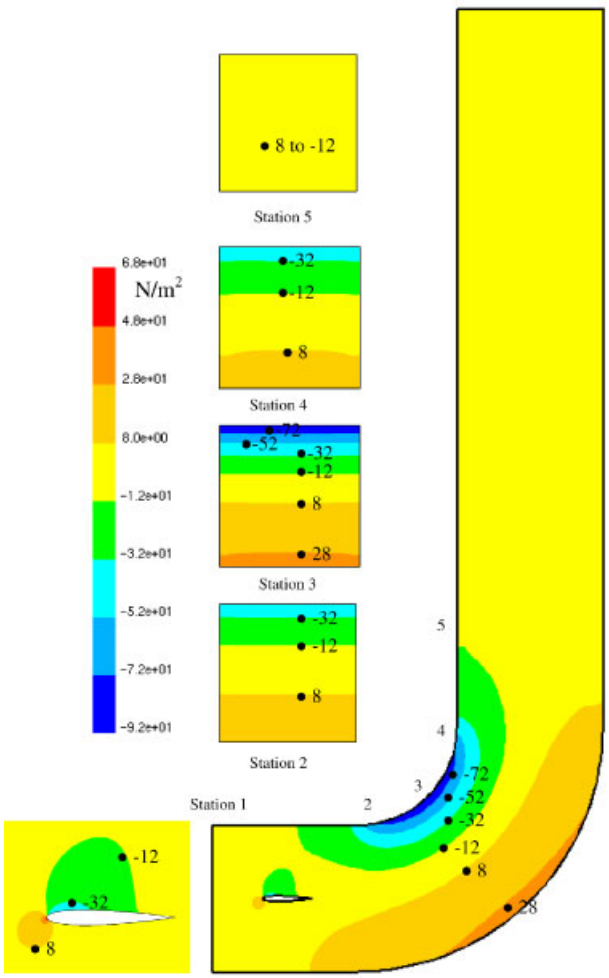


Figure 3. Computed pressure distribution ($N/m^2$). Pressure is relative to the reference value at station 1.

A detailed description of the boundary layers on the concave and convex walls is given in an earlier study [20]. The boundary layer on the convex wall remains thin, while on the concave wall reaches a thickness of about 20% of the duct height at station 4. The boundary layers on the sidewalls also remain thin. There is therefore a large portion of the cross-sectional area of the duct which is unaffected by the developing boundary layers on the bend walls. This region has a turbulence intensity of less than 0.3% and will be referred to as the *inviscid* region. The development of the boundary layers can be seen in Figure 4. This figure shows significant thickening of the boundary layer downstream of station 4 on the convex wall, but no flow separation and reversal were predicted in this region. However, experimental visualization of the flow in the bend showed intermittent separation on the convex wall at station 4 and

Copyright © 2005 John Wiley & Sons, Ltd. 

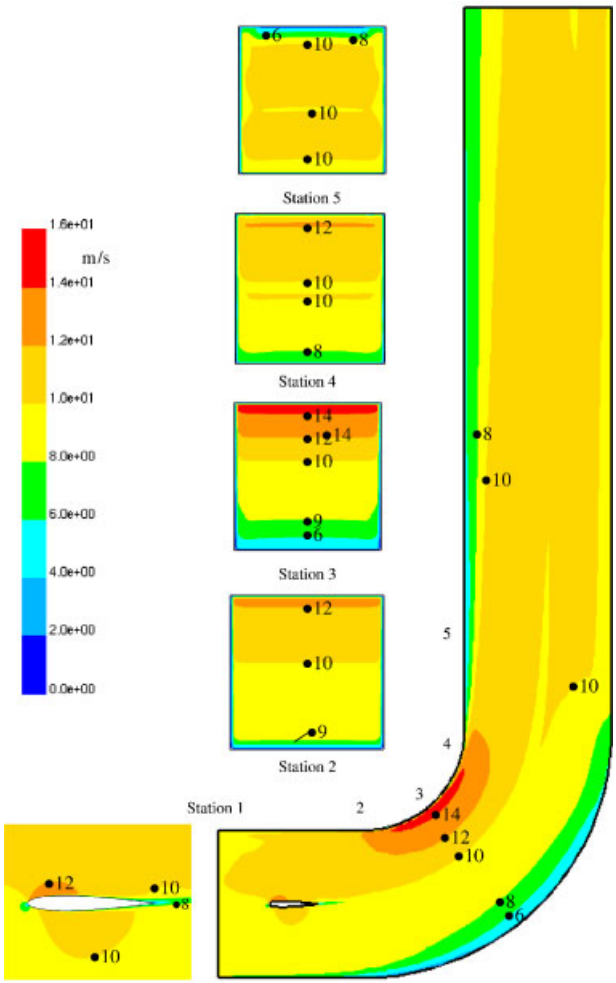


Figure 4. Computed velocity magnitude (m/s).

subsequent reattachment before station 5, but no stationary separation bubble was evident. Due to this, turbulence also increased significantly. The effect of this flow condition is also apparent in the static pressure distribution on the duct walls shown in Figure 5, where there is very good agreement with experiment up to about station 4, beyond which significant deviations occur, especially on the convex wall. The inability to predict these experimental conditions points to more general and difficult problem of prediction of separation from a continuous curved surface, compared with separation from a discontinuous surface. The conditions present on the convex wall are difficult to predict due to the boundary layer being at the point of separation and a fully separated region has not been established. It should however be pointed out that, as was noted above, due to restricted computer resources, it was not possible to employ a very fine grid near the bend walls, for the effective implementation of the two-layer model.

Copyright © 2005 John Wiley & Sons, Ltd. 

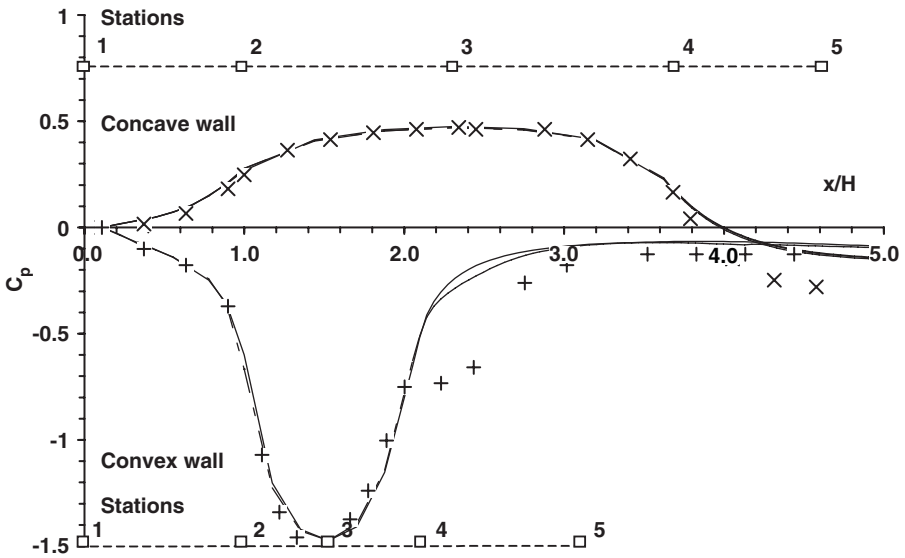


Figure 5. Pressure coefficient on the concave and convex walls of the duct x, + experiment, —RSM, —— standard $k$–$\varepsilon$, - - - realizable $k$–$\varepsilon$, - · - · RNG $k$–$\varepsilon$.

In the following results, therefore, direct comparison of the experimental and predicted results is confined to stations 2–4.

### 6.2. *Pressure distribution on the duct walls*

Figure 5 shows that, computationally, the effect of turbulence model on the pressure distribution is negligible, as all models predict the pressure coefficient with the same level of accuracy. There is an overall irrecoverable pressure loss between stations 1 and 5, evident from the negative values of pressure coefficient at station 5. Experimentally, there is a greater pressure drop due to additional losses not accounted for in the prediction.

### 6.3. *Streamwise velocity and wake parameters*

Figure 6(a) shows the profiles of streamwise velocity. The position of the predicted wake is always higher than that in the experiment. The wake is first shifted towards the convex wall at stations 2 and 3 and then towards the concave wall at station 4. The direction of this shift is correctly predicted. There is particularly a good agreement in the inviscid region. The boundary layer regions are also well predicted.

Closer comparison of the wake profiles can be made when they are aligned with respect to the wake centreline as shown in Figures 6(b)–(d). There are noticeable differences between prediction and experiment. It appears that experimentally there is greater mixing and interaction with the outer inviscid flow, resulting in more uniform velocity in the wake and thus smaller velocity defect. For the velocity defect, the largest discrepancy with experiment is produced by the RSM. Comparing the predicted profiles with each other, show little difference between them at station 2. The differences, however, enhance as the wake develops. The

Copyright © 2005 John Wiley & Sons, Ltd. 

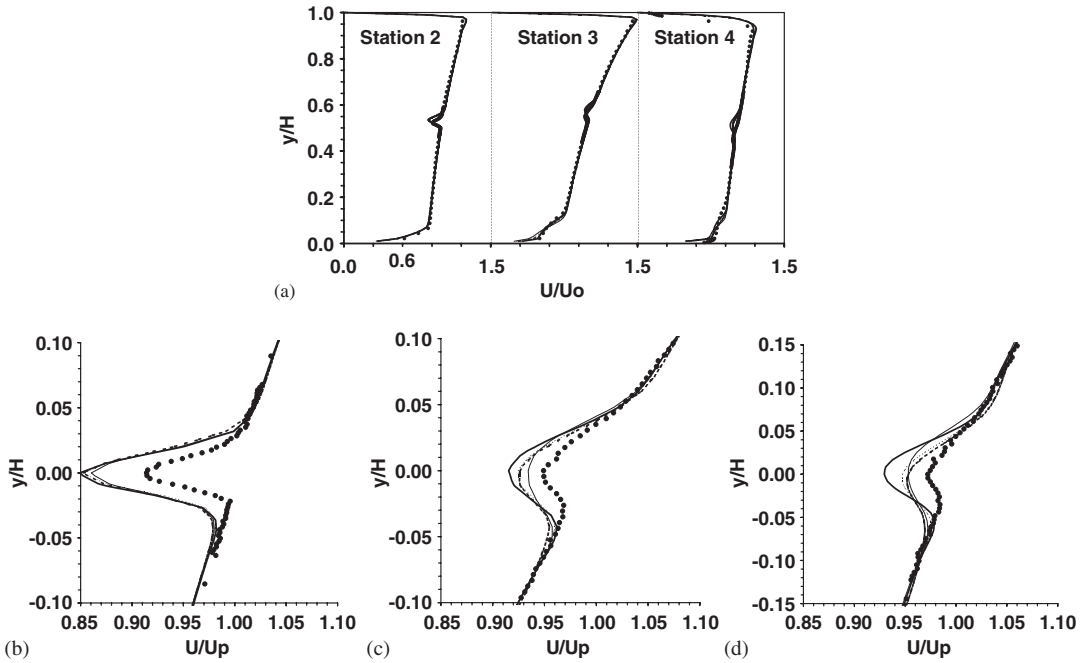


Figure 6. Comparison of predicted streamwise velocity with experiment: (a) across the duct; (b)–(d) wake region; (b) station 2, (c) station 3, (d) station 4. • Experiment, — RSM, ··· standard $k$–$\varepsilon$, — realizable $k$–$\varepsilon$, - - - - RNG $k$–$\varepsilon$. In panels (b)–(d), distance $y$ is the adjusted distance, such that the profiles are aligned with respect to the wake centerline for velocity. In panel (a), the profiles are as measured and predicted with $y$ measured from the lower wall.

$k$–$\varepsilon$ models produce generally similar predictions. The profiles of the standard $k$–$\varepsilon$ and RNG $k$–$\varepsilon$ are in closer agreement with each other than the realizable $k$–$\varepsilon$, which produces results closer to the experimental values at stations 2 and 3. All models predict the position of the wake edge on the inner side better than the position of the wake edge on the outer side. The RSM, however, predicts the wake edge on the outer side closer to the experimental values.

The simulations carried out by Narasimhan *et al.* [13] and Tulapurkara *et al.* [15] using the $k$–$\varepsilon$ model produced generally better comparisons with their own experimental data for the wake of the airfoil, than achieved in the present study. The reason may be attributed to the placement of the boundary conditions at the trailing edge of the airfoil and by setting other conditions as was pointed out earlier. The present study includes the prediction of the boundary layers on the airfoil in the simulation, which introduces the added complexity of dealing with laminar flow near the leading edge of the airfoil and then laminar to turbulent transition as the flow approaches the trailing edge. As was noted earlier, we matched, at station 2, the profiles of turbulence energy in the inviscid region in order to set the length scale. The reason for not following fully the approach of Narasimhan *et al.* and Tulapurkara *et al.* is that, we believe such techniques are difficult to employ in a practical engineering environment, and the usual approach would be to place the boundary conditions upstream of the airfoil where the flow can be more conveniently defined.

Copyright © 2005 John Wiley & Sons, Ltd. 

An accurate prediction of the boundary layer flow on the airfoil depends on the degree of applicability of both the near wall model, which is applied to the flow region in the immediate vicinity of the wall, and also to the turbulence model applied to the flow beyond this region. Both these models are expected to work better for developed turbulent flows. Due to this, in contrast to the simulations of Narasimhan *et al.* and Tulapurkara *et al.*, the calculation of the wake starts with differences between prediction and experiment at the trailing edge, which is believed to be at least partly responsible for the differences in the wake. A full study of the boundary layer development on the airfoil was beyond the scope of the present experimental and numerical investigation. However, experiments carried out by Onura [19] on the upper surface of the same airfoil will be used in the following discussion of the results to provide some information on the state of the flow on the upper surface of the airfoil. No data was available for the lower surface.

Figure 7 shows the profiles of the predicted velocity magnitude using RSM at several locations on the airfoil. It can be seen that the boundary layer thickness is very thin up to the maximum thickness of the airfoil, $t$. The boundary layer thickness then increases and reaches a thickness of about $0.8t$ at the trailing edge. Figure 8 shows a comparison of the predicted profile of velocity magnitude at 26 mm upstream of the trailing edge with the measurements of Onura [19]. The results show reasonable agreement between the two results. The predicted boundary layer shows greater thickness and the difference in the overall shape of the profiles are consistent with the differences evident in Figure 6(b).

Two wake parameters can be calculated from the profiles in Figure 6. These are the total wake half-width and maximum velocity defect, presented in Figures 9 and 10, respectively. There is a fair agreement for the wake half-width, but the differences in the predicted wake profiles have resulted in large differences in the maximum velocity defect. All models over

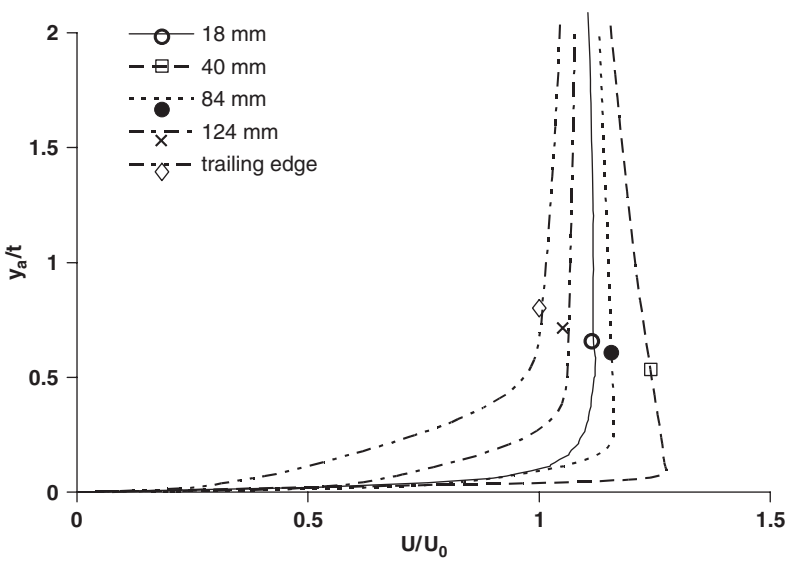


Figure 7. Profiles of velocity magnitude on the upper surface of the airfoil. Distances are measured from the leading edge, along the chord.

Copyright © 2005 John Wiley & Sons, Ltd. 

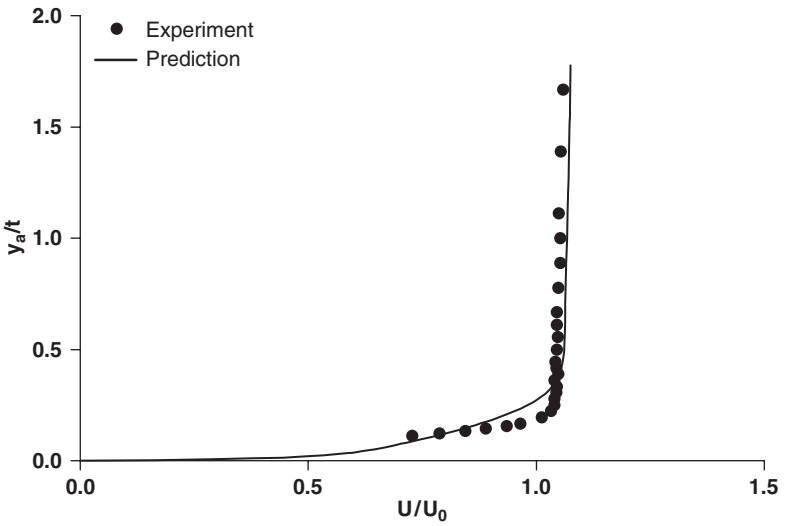


Figure 8. Comparison of predicted velocity magnitude with experimental data [19] on the airfoil at 26 mm upstream of the trailing edge.

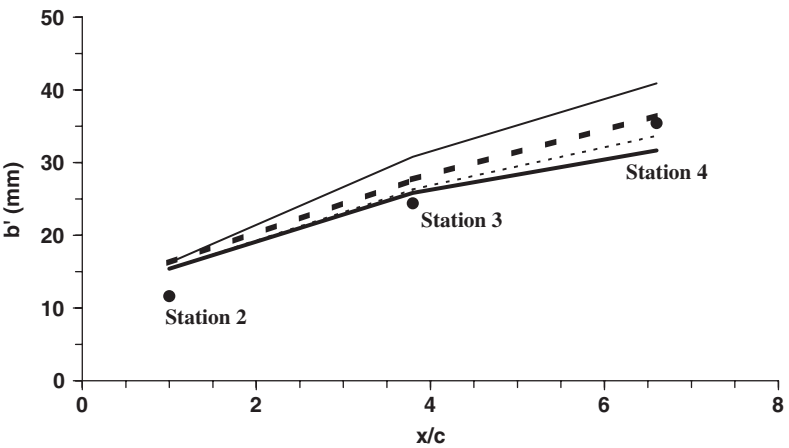


Figure 9. Comparison of total wake half-width with experiment.

predict the maximum velocity defect and the wake half-width. The wake half-width increases in the streamwise direction. Experimentally, this increase is nearly linear, while computationally the growth is steeper between stations 2 and 3 than between stations 3 and 4. The maximum velocity defect decreases in the streamwise direction, and this decrease is also more linear experimentally.

Copyright © 2005 John Wiley & Sons, Ltd. 

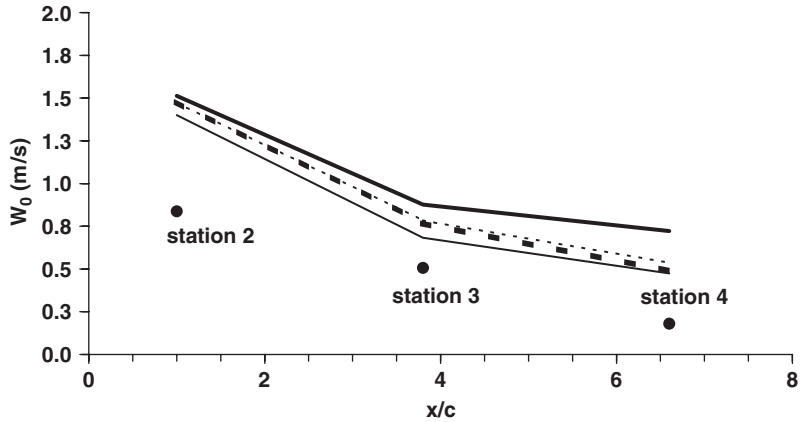


Figure 10. Comparison of predicted maximum velocity defect with experiment. • Experiment, —— RSM, - - - standard $k$–$\varepsilon$, — realizable $k$–$\varepsilon$, - - - RNG $k$–$\varepsilon$.

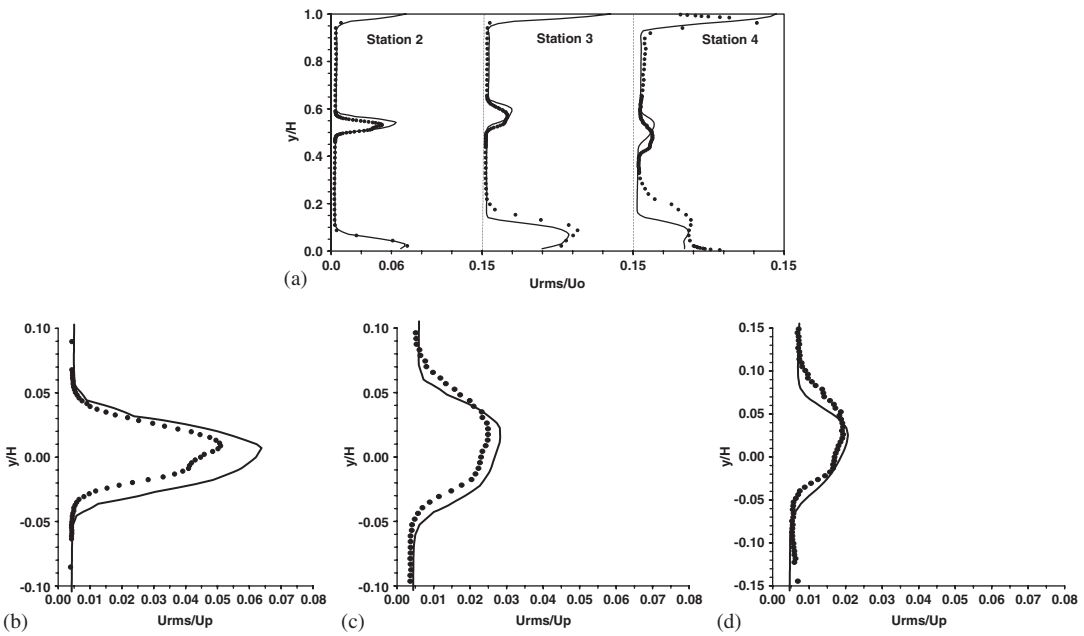


Figure 11. Comparison of predicted streamwise intensity with experiment. • Experiment, — RSM. See also caption in Figure 6.

### 6.4. *Turbulence intensity*

The profiles of streamwise intensity are shown in Figure 11(a). There is a general agreement between the profiles in the inviscid region at stations 2–4. Also, the general shape of the boundary layer profile and increased turbulence activity on the concave wall, is well predicted.

Copyright © 2005 John Wiley & Sons, Ltd. 

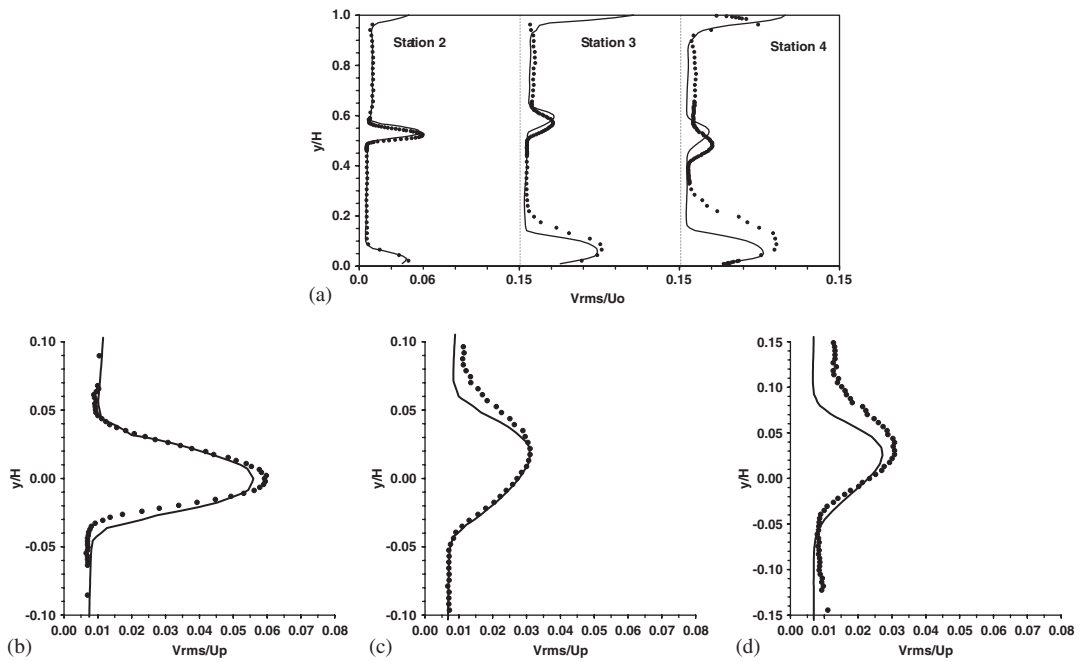


Figure 12. Comparison of predicted normal intensity with experiment. • Experiment, — RSM. See also caption in Figure 6.

The agreement is better at stations 2 and 3 on the concave wall, but the differences increase as the boundary layer develops. The experimental profiles show a greater width of the flow in the duct is affected by the boundary layer development on the concave wall.

The profiles of streamwise intensity, aligned with respect to the wake centreline for velocity ($y/H = 0.0$) are shown in Figures 11(b)–(d). These results are obtained using the RSM, since the $k$–$\varepsilon$ models do not predict individual turbulence intensities. Three main comparisons can be made when referring to this figure. Firstly, the overall shape of the profile and the expected characteristics. Secondly, the magnitude of the intensity and the peak value, and thirdly, since these profiles are aligned with respect to the wake centreline for velocity, their relative positions with respect to this datum can be compared. The shape of the experimental profile is well predicted at all stations. The turbulence intensity is enhanced on the inner side of the wake and is reduced on the outer side. This effect of curvature on turbulence is therefore correctly predicted. Both profiles place the peak in intensity at a higher position than the wake centreline for velocity. There is an over prediction of the intensity over the width of the wake at station 2. At stations 3 and 4, however, the over prediction remains on the outer side of the wake, whereas the intensity is now underpredicted on the inner side.

Figures 12 and 13 show the profiles of normal and spanwise intensities, respectively. Again there is a general agreement between the main characteristics of the predicted and experimental profiles. The aligned profiles show a better match on the outer side of the wake. Experimentally, the wake engulfs greater region of increased turbulence activity at stations 3 and 4. For the normal intensity (Figure 12(a)), the overall flow features across the duct are

Copyright © 2005 John Wiley & Sons, Ltd. 

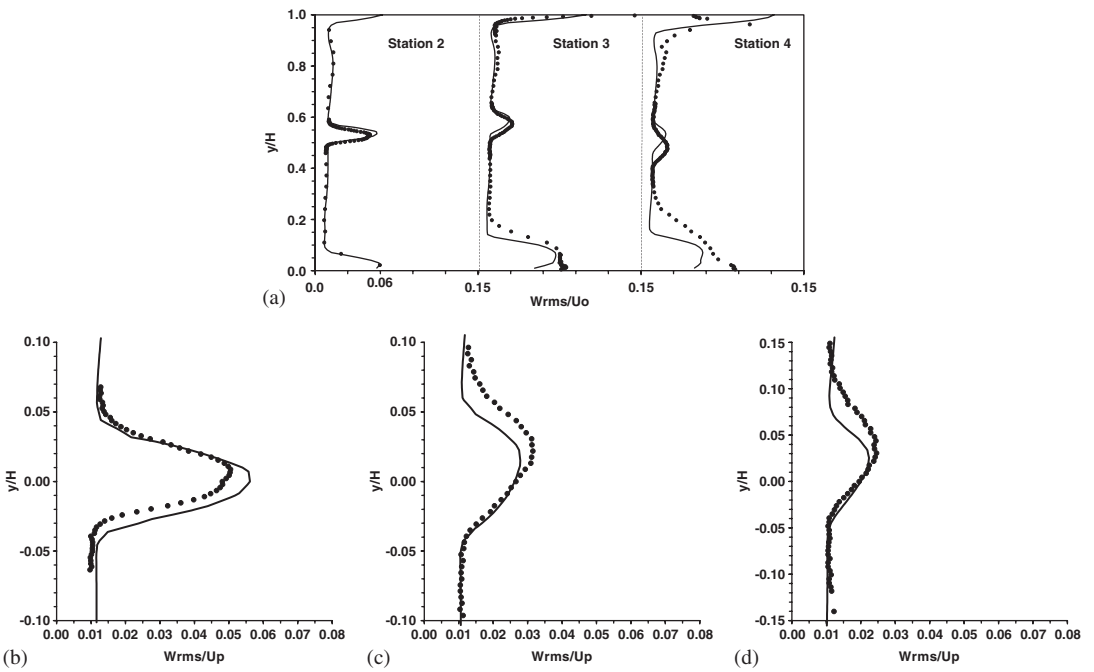


Figure 13. Comparison of predicted spanwise intensity with experiment. • Experiment, — RSM. See also caption in Figure 6.

also in good agreement, except in the inviscid region on the convex side, which shows under prediction. The profiles of spanwise intensity (Figure 13(a)) show greater differences between experiment and prediction in the boundary layer on the concave wall.

### 6.5. *Turbulence energy*

Figure 14 shows the profiles of turbulence kinetic energy. In this figure the profiles predicted by all four models are included for comparison. Overall, the RSM produces the closest agreement between prediction and experiment, although there is noticeable overprediction of turbulence energy at station 2 and underprediction at stations 3 and 4. The $k$–$\varepsilon$ models overpredict turbulence activity in the wake region at all stations. The values in the inviscid region are matched better by the RSM, while all the $k$–$\varepsilon$ models again overpredict the turbulence activity in this region, in particular the standard $k$–$\varepsilon$ model, which gives very high values on the convex side of the bend. Comparing the $k$–$\varepsilon$ models with each other, the RNG $k$–$\varepsilon$ is able to capture the experimental profile more closely and predicts a smaller peak. In fact the level of agreement obtained for the RNG $k$–$\varepsilon$ is about the same as the RSM model, except that it predicts greater turbulence energy than the RSM does. The predicted profiles by the $k$–$\varepsilon$ models are in better agreement with each other at station 2, but differences enhance as the wake develops.

The boundary layer development on the airfoil was referred to above (Figure 7). The corresponding profiles of turbulence energy are shown in Figure 15. As can be seen some

Copyright © 2005 John Wiley & Sons, Ltd. 

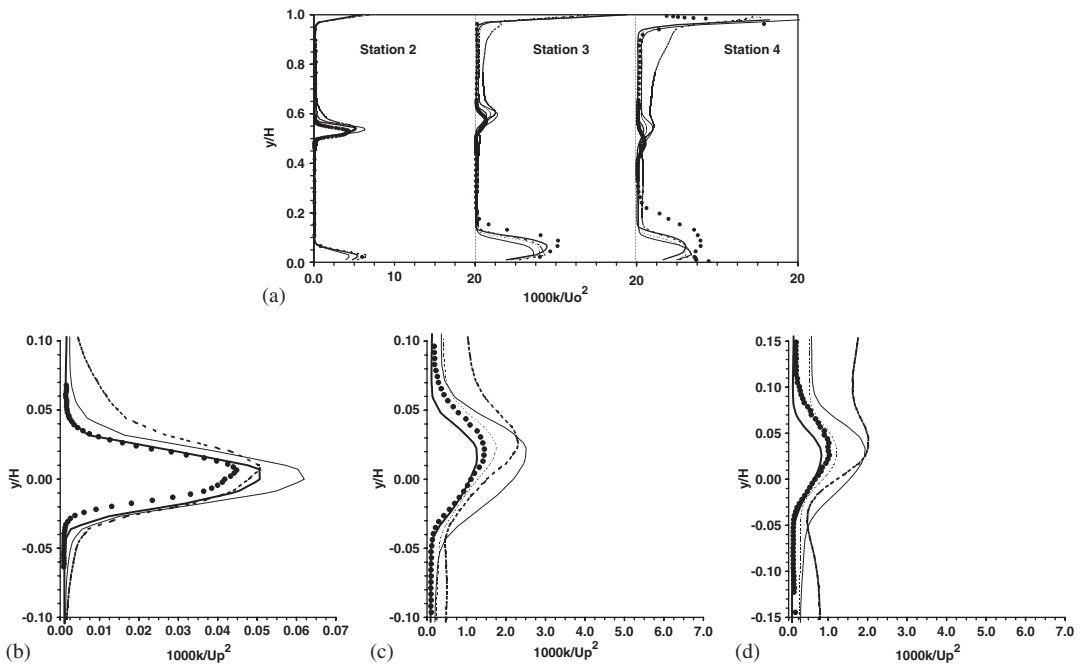


Figure 14. Comparison of predicted turbulence energy with experiment.
See rest of caption in Figure 6.

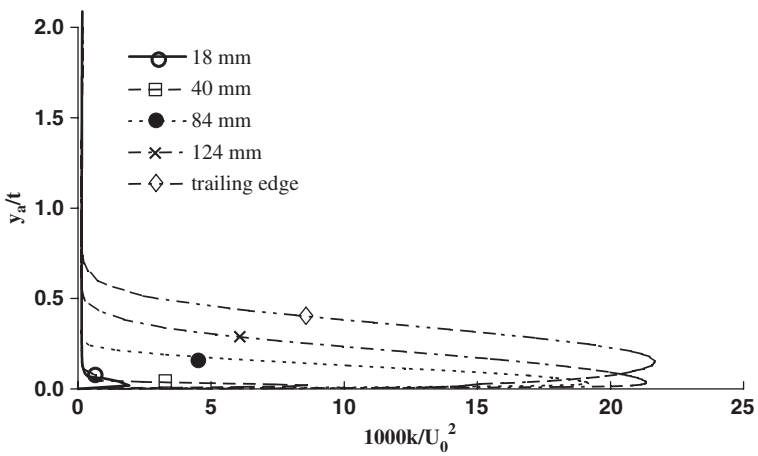


Figure 15. Turbulence energy profiles on the upper surface of the airfoil. Distances are measured from the leading edge, along the chord.

turbulence activity is predicted even at the first measurement point located at 18 mm downstream of the front stagnation point, but the activity is limited to only a very small region close to the wall. Taking all the turbulence intensities to be equal, so that they may be approx-

Copyright © 2005 John Wiley & Sons, Ltd. 

imated from the value of $k$, the maximum turbulence intensity is about 3.6%, which is much greater than the free stream intensity of less than 0.5%. The value of $k$ increases further, but at 40 mm from the leading edge the turbulence activity is still confined to a very thin region next to the wall. Beyond the maximum thickness, however, the value of $k$ and the thickness of flow region involved have increased substantially. Onura [19] did not measure the spanwise intensity on the airfoil, but comparisons with the measured streamwise and normal intensities at 124 mm ($0.83c$) from the leading edge are shown in Figures 16 and 17, respectively. The

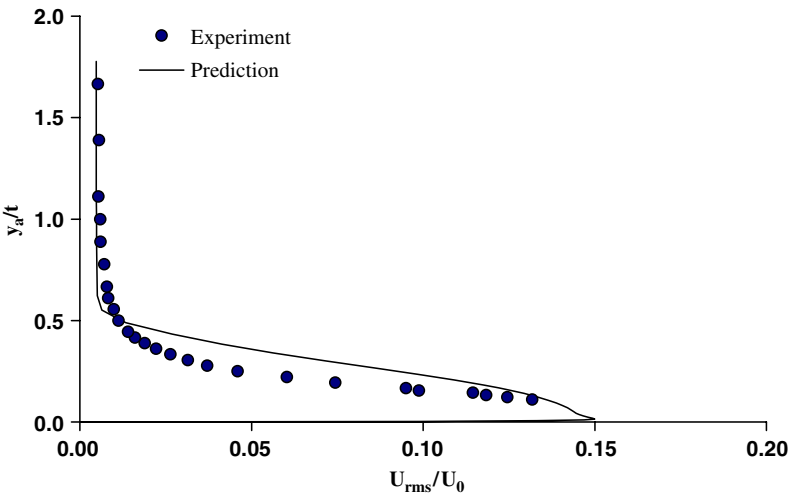


Figure 16. Comparison of predicted streamwise intensity on the upper surface of the airfoil with experimental data [19].

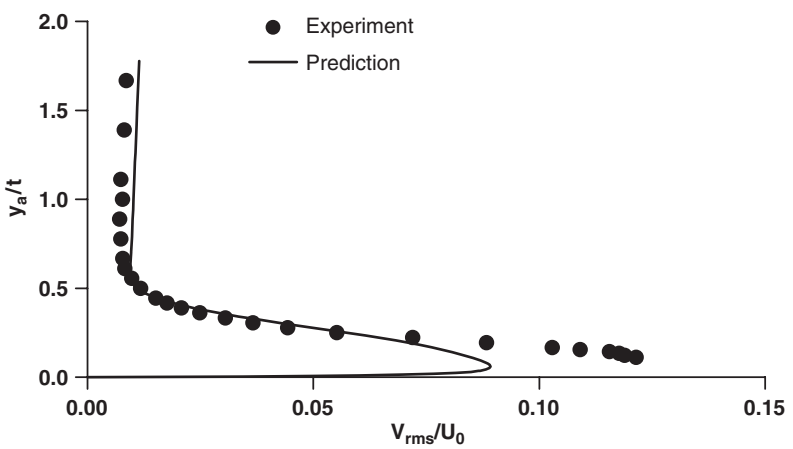


Figure 17. Comparison of the predicted normal intensity on the airfoil with experimental data of Onura [19].

Copyright © 2005 John Wiley & Sons, Ltd. 

experimental results indicate occurrence of boundary layer transition upstream of this measurement point. There is a fair agreement between prediction and experiment, which gives some support to the use of the two-layer model and the RSM. However, as was noted above the application of the near wall model and the turbulence model is expected to lead to differences between prediction and experiment for the boundary layer flow on the airfoil. Additionally, from the results obtained, it can be also said that the prediction has not provided evidence of any separation bubble on the airfoil.

Referring back to Figure 11 for streamwise intensity in the wake and comparing the results with those of Figure 16 for the streamwise intensity on the airfoil upper surface shows consistency between the two results. The over prediction of intensity in the boundary layer edge region on the airfoil is consistent with the over prediction of the intensity on the inner side of the wake at station 2. Similarly good matching of the normal intensity displayed in Figure 12(b) is consistent with good agreement obtained in Figure 17. It appears therefore that as stated above some of the differences between prediction and experiment in the wake originate from the differences on the airfoil.

### 6.6. *Turbulence shear stress* $-\overline{uv}$

The profiles of Reynolds stress $-\overline{uv}$ are shown in Figure 18. Experimentally, the shear stress profile exhibits two peaks of different signs and magnitudes. The shear stress is enhanced on the inner side due to the effect of curvature, whereas it is suppressed on the outer side. There

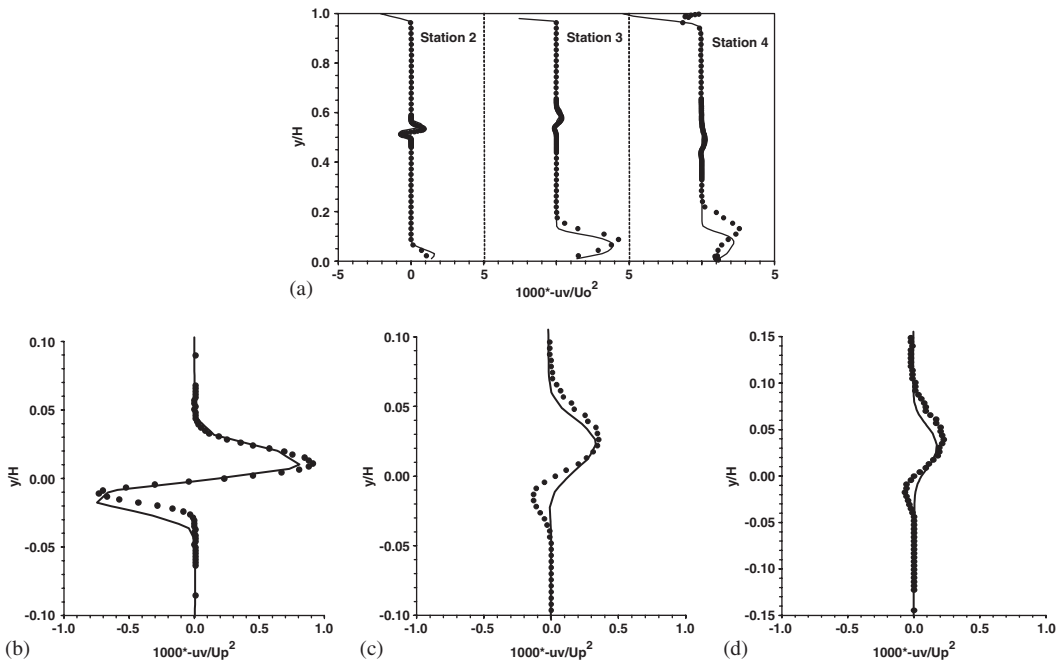


Figure 18. Comparison of turbulence shear stress with experiment. • Experiment, — RSM. See also caption in Figure 6.

Copyright © 2005 John Wiley & Sons, Ltd. 

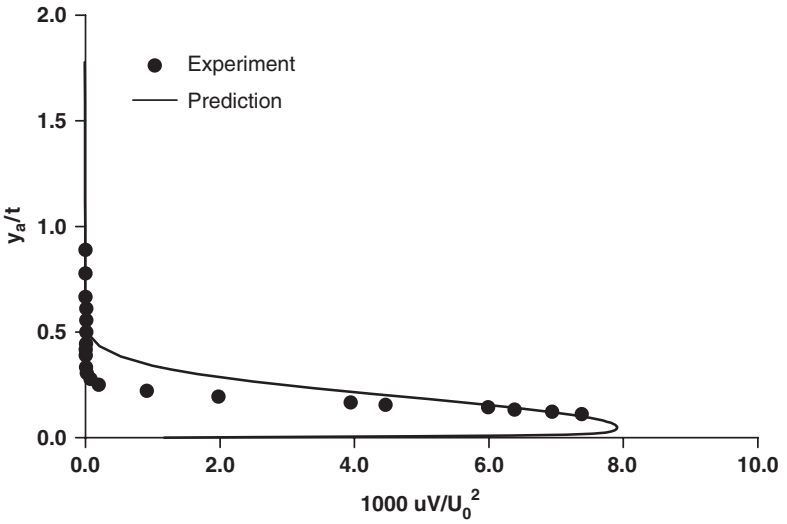


Figure 19. Comparison of the predicted turbulence shear stress on the upper surface of the airfoil with experimental data [19].

is a good agreement at station 2 between the two profiles. At stations 3 and 4 the larger peak on the inner side is also in good agreement with the experimental results. The suppression of shear stress on the outer side, however, is overpredicted to such a degree that the negative peak is indistinguishable. It therefore appears that the model has greater difficulty to deal with the stabilizing effect of curvature on shear stress than the destabilizing effect. Comparisons have also been made with the experimental data of Onura [19] in Figure 19, which again shows reasonable agreement.

The different effects of curvature on the inner side from that on the outerside can be deduced from the inspection of the production term in the differential equations of turbulence intensities and turbulence stresses [28] (Table III).

In the $\overline{u^2}$-equation, the production term includes

$$-\overline{uv}\left[\left(1+\frac{n}{R}\right)\frac{\partial U}{\partial n}-\frac{U}{R}\right]$$

On the inner side $-\overline{uv}>0$, $\partial U/\partial n>0$, whereas on the outer side $-\overline{uv}<0$, $\partial U/\partial n<0$. Since $U/R<0$ on both sides, the first term $-\overline{uv}[(1+(n/R))(\partial U/\partial n)]$ makes a positive contribution to the production term on both the inner and outer sides. The second term $-\overline{uv}[-U/R]$ is positive on the inner side and makes a further positive contribution to the production of turbulence intensity, whereas it is negative on the outerside side, thus reducing the production.

In the $\overline{v^2}$-equation, the production term includes $-\overline{uv}\,\partial V/\partial s$, where $\partial V/\partial s=-U/R$ [28]. Again due to the change in the sign of $-\overline{uv}$ at the wake symmetry line, this term is positive in the inner side and negative on the outer side, producing the asymmetry in the profile of the normal turbulence intensity.

There is no production of $\overline{w^2}$, however, the profile of spanwise intensity shows an asymmetry in the profile. The radius of curvature only appears in the diffusion term involving a

Copyright © 2005 John Wiley & Sons, Ltd. 

higher order term. The effect of curvature on the spanwise turbulence intensity can therefore be attributed to this term.

In the $\overline{uv}$-equation, the main production term is

$$\overline{u^2}\left(\frac{\partial V}{\partial s}-\frac{U}{R}\right)+\overline{v^2}\left(1+\frac{n}{R}\right)\frac{\partial U}{\partial n}$$

Since $\partial V/\partial s = -U/R$, the first term makes positive contribution to the production of $-\overline{uv}$ on both inner and outer sides. The second term, however, makes a positive contribution on the inner side (since $\partial U/\partial n > 0$) and a negative contribution on the outer side, explaining the different effects of curvature on turbulence shear stress.

## 7. CONCLUSIONS

There is general qualitative agreement between the predictions and the experimental data for overall features of the mean flow and profiles of turbulence quantities in the wake, in the inviscid region and in the boundary layers. Differences are evident when the exact values are compared, and this is where the inherent differences in the turbulence models manifest themselves.

The overall variations of mean and turbulence properties in the concave boundary layer were well predicted, although experimentally the boundary layer engulfed greater width of the flow.

There was agreement between prediction and experiment for the pressure coefficient distribution on the duct walls up to station 4. There were insignificant differences between the profiles predicted by all models.

The experiments suggest that the wake position within the duct does not coincide with the duct centreline, as it is first shifted towards the convex wall and then towards the concave wall. This was predicted correctly, although the exact position did not match closely. The velocity in the wake was under predicted, leading to significant differences between the predicted and measured maximum velocity defect. The computations using the RSM showed the greatest discrepancy for the velocity defect, in contrast to generally better predictions of the turbulence parameters.

For a wake subjected to curvature, turbulence is increased on the inner side of the wake, but is reduced on the outer side. All models predicted this correctly. The turbulence shear stress $-\overline{u'v'}$ showed two peaks of different signs, with the larger peak being located on the inner side. The prediction of enhancement of shear stress on the inner side by the RSM was in good agreement with experiment, but suppression of shear stress on the outer side was overpredicted. The closest agreement for turbulence energy was also obtained by the RSM.

The results showed that the improved $k$–$\varepsilon$ models (RNG and realizable) provided better comparisons with the experimental data than the standard $k$–$\varepsilon$ model. Comparing the RNG and realizable models, the RNG model produced results, which were generally closer to the experimental data.

Some of the differences between prediction and experiment may be attributed to the difficulty in modelling the boundary layers on the airfoil, which rely on the accuracy of the near-wall treatment and the turbulence model. The correct prediction of the boundary layers on the airfoil is therefore important in order to obtain better predictions in the wake.

Copyright © 2005 John Wiley & Sons, Ltd. 

## NOMENCLATURE

| | |
|---|---|
| $b$ | wake half-width |
| $b'$ | total wake half-width |
| $C_p$ | pressure coefficient, $C_p = (p - p_0)/(0.5\rho U_0^2)$ |
| $c$ | airfoil chord length |
| $H$ | duct height |
| $k$ | turbulence kinetic energy |
| $l$ | length scale |
| $p$ | static-pressure |
| $p_0$ | reference pressure |
| $R$ | radius of curvature |
| $t$ | airfoil maximum thickness |
| $U_0$ | mainstream velocity at station 1 |
| $U_P$ | wake centreline potential velocity |
| $U_{\text{rms}}$ | turbulence intensity, $U_{\text{rms}} = \sqrt{\overline{u^2}}$ |
| $U_i$ | velocity components |
| $U$, $V$ | time-averaged streamwise and normal velocity components, respectively |
| $u, v, w$ | fluctuating velocity components in $x$-, $y$- and $z$-directions |
| $\overline{u_i v_j}$ | turbulence shear stresses |
| $W_0$ | maximum velocity defect |
| $x$ | streamwise distance measured from station 1 |
| $y$ | normal distance from the lower wall (concave) of the bend |
| $y_a$ | vertical distance from the upper surface of the airfoil |
| $y^+$ | non-dimensional distance from the wall |
| $z$ | spanwise distance measured from the side wall |

### *Greek letters*

| | |
|---|---|
| $\varepsilon$ | energy dissipation rate |
| $\mu$ | dynamic viscosity |
| $\mu_t$ | turbulent viscosity |
| $\mu_{\text{eff}}$ | effective viscosity |
| $\rho$ | density |


## ACKNOWLEDGEMENTS

The study was carried out using FLUENT 5 and the mesh generator GAMBIT under an academic license.


## REFERENCES


1. Chevray R, Kovasznay LSG. Turbulence measurements in the wake of a thin flat plate. *AIAA Journal* 1969; **7**:1641–1643.
2. Savil AM. The turbulence structure of a highly curved two-dimensional wake. In *Proceedings of the IUTAM Symposium on Complex Turbulent Flows*, Dumas R, Fulachier F (eds). Springer: Berlin, 1983; 185–197.
3. Koyama HS. Effects of streamline curvature on laminar and turbulent wakes. *Proceedings of the Fourth Symposium on Turbulent Shear Flows*. University of Karlsruhe: Karlsruhe, Germany, 1983; 141–155.


Copyright © 2005 John Wiley & Sons, Ltd. 

4. Nakayama V. Curvature and pressure-gradient effects on a small-defect wake. *Journal of Fluid Mechanics* 1987; **175**:215–246.
5. Ramjee V, Tulapurkara EG, Rajasekar R. Development of airfoil wake in a longitudinally curved stream. *AIAA Journal* 1988; **26**(8):948–953.
6. Ramjee V, Neelakandan D. Development of wake of a rectangular cylinder in a curved stream. *Experiments in Fluids* 1989; **7**:395–399.
7. Ramjee V, Neelakandan D. Curvature effects on the wake of an airfoil and other bodies. *Fluid Dynamics Research* 1990; **6**:1–13.
8. Tulapurkara EG, Ramjee V, George J. Development of wake in presence of both curvature and pressure gradient. *Boundary Layer and Free Shear Flows*, *Transactions of the ASME* 1994; **184**:195–202.
9. Tulapurkara EG, Ramjee V, Jacob G. Development of a bluff body wake under the combined influence of curvature and pressure gradient. *Experiments in Fluids* 1995; **18**:311–318.
10. John J, Schobeiri MT. Development of a two-dimensional turbulent wake in a curved channel with a positive streamwise pressure gradient. *Journal of Fluids Engineering*, *Transactions of the ASME* 1996; **118**:292–299.
11. Schobeiri MT, John J, Pappu K. Development of two-dimensional wakes within curved channels: theoretical framework and experimental investigation. *Journal of Fluids Engineering*, *Transactions of the ASME* 1996; **118**:506–518.
12. Starke AR, Henkes RAWM, Tummers MJ. Effects of curvature and pressure gradient on a turbulent near wake. *Experimental Thermal and Fluid Science* 1999; **19**:49–56.
13. Narasimhan JL, Ramjee V, Diwaakar P, Philip M, Tulapurkara EG. Prediction of wake in a curved duct. *International Journal for Numerical Methods in Fluids* 1991; **33**:907–916.
14. Leschziner MA, Rodi W. Calculation of annular and twin parallel jets using various discretization schemes and turbulence-model variations. *Journal of Fluids Engineering* (ASME) 1981; **103**:352–360.
15. Tulapurkara EG, Ramjee V, Jacob G. Prediction of aerofoil wake subjected to the effects of curvature and pressure gradient. *International Journal for Numerical Methods in Fluids* 1996; **22**:29–41.
16. Humphrey JAC, Pourahmadi F. Prediction of curved channel flow with an extended $k$–$\varepsilon$ model of turbulence. *AIAA Journal* 1983; **21**:1365–1373.
17. Piradeepan N. An experimental and numerical investigation of a turbulent airfoil wake in a 90° curved duct. *PhD Thesis*, Brunel University, Uxbridge, U.K., 2002.
18. Piradeepan N, Mokhtarzadeh-Dehghan MR. Measurements of mean and turbulence quantities in the curved wake of an airfoil. *Experimental Thermal and Fluid Science* 2005; **29**:239–252.
19. Onura O. Experimental investigation of the turbulent quantities in the near wake region, behind a NACA 0012 aerofoil. Department of Mechanical Engineering, Brunel University, Uxbridge, U.K., 2003.
20. Mokhtarzadeh-Dehghan MR, Yuan YM. Measurements of turbulence quantities and bursting period in developing turbulent boundary layers on the concave and convex walls of a 90° square bend. *Experimental Thermal and Fluid Science* 2002; **27**:59–75.
21. FLUENT 5 User's guide. Fluent Incorporated, Centerra Resource Park, 10 Cavendish Court, Lebanon, NH 03766-1442, U.S.A.
22. Yakhot V, Orszag SA. Renormalization group analysis of turbulence: I. Basic theory. *Journal of Scientific Computing* 1986; **1**(1):1–51.
23. Shih T-H, Liou WW, Shabbir A, Yang Z, Zhu J. A new $k$–$\varepsilon$ eddy viscosity model for high Reynolds number turbulent flows. *Computers and Fluids* 1995; **24**(3):227–238.
24. Hanjalić K. Advanced turbulence closure models: a review of current status and future prospects. *International Journal of Heat and Fluid Flow* 1994; **15**(3):178–203.
25. Gibson MM, Rodi W. A Reynolds-stress closure model of turbulence applied to the calculation of a highly curved mixing layer. *Journal of Fluid Mechanics* 1981; **103**:161–182.
26. Chen HC, Patel VC. Near-wall turbulence models for complex flows including separation. *AIAA Journal* 1988; **26**(6):641–648.
27. Leonard BP. A stable and accurate convective modelling procedure based on quadratic upstream interpolation. *Computer Methods in Applied Mechanics and Engineering* 1979; **19**:59–98.
28. Weygandt JH, Mehta RD. Three-dimensional structure of straight and curved plane wakes. *Journal of Fluid Mechanics* 1995; **282**:279–311.

Copyright © 2005 John Wiley & Sons, Ltd. 